Strongly exchange coupled core|shell nanoparticles with high magnetic anisotropy : a strategy toward rare-earth-free permanent magnets

Reference:

Lottini E., Lopez-Ortega A., Bertoni G., Turner Stuart, Meledina Maria, Van Tendeloo Gustaaf, de Fernandez C. Julian, Sangregorio C..- Strongly exchange coupled core|shell nanoparticles with high magnetic anisotropy : a strategy toward rare-earth-free permanent magnets

Chemistry of materials - ISSN 0897-4756 - 28:12(2016), p. 4214-4222

Full text (Publisher's DOI): http://dx.doi.org/doi:10.1021/ACS.CHEMMATER.6B00623

To cite this reference: http://hdl.handle.net/10067/1340840151162165141

Strongly exchange coupled core|shell nanoparticles with high magnetic anisotropy: a strategy towards Rare Earth - free permanent magnets

E. Lottini[†], A. López-Ortega[†*], G. Bertoni[‡], S. Turner[§], M. Meledina[§], G. Van Tendeloo[§], C. de Julián Fernández[‡], C. Sangregorio[⊥*]

[†]*INSTM and Università degli Studi di Firenze, Sesto Fiorentino (Firenze), Italy.*

[‡]*CNR-IMEM, Parma, Italy.*

[§]*EMAT, University of Antwerp, Belgium.*

[⊥]*INSTM and CNR-ICCOM, Sesto Fiorentino (Firenze), Italy.*

ABSTRACT

Antiferromagnetic(AFM)|ferrimagnetic(FiM) core|shell (CS) nanoparticles (NPs) of formula $Co_{0.3}Fe_{0.7}O|Co_{0.6}Fe_{2.4}O_4$ with mean diameter from 6 to 18 nm have been synthesized through a one-pot thermal decomposition process. The CS structure has been generated by topotaxial oxidation of the core region, leading to the formation of a highly monodisperse single inverted AFM|FiM CS system with variable AFM-core diameter and constant FiM-shell thickness (~2 nm). The sharp interface, the high structural matching between both phases and the good crystallinity of the AFM material have been structurally demonstrated and are corroborated by the robust exchange-coupling between AFM and FiM phases, which gives rise to one among the largest exchange bias (H_E) values ever reported for CS NPs (8.6 kOe) and to a strongly enhanced coercive field (H_C). In addition, the investigation of the magnetic properties as a function of the AFM-core size (d_{AFM}), revealed a non-monotonous trend of both H_C and H_E, which display a maximum value for d_{AFM} = 5 nm (19.3 and 8.6 kOe, respectively). These properties induce a huge improvement of the capability of storing energy of the material, a result which suggests that the combination of highly anisotropic AFM|FiM

materials can be an efficient strategy towards the realization of novel Rare Earth-free permanent magnets.

INTRODUCTION

The ability to control the assembly of materials with different properties into complex nanoscale architectures has recently provided a formidable thrust towards the discovery and unraveling of novel exciting physical phenomena, often of high technological impact. Indeed, the full exploitation of such effects relies on the capability of a fine control of the interface shared by the coupled materials, and on the ability to independently vary every single parameter involved.[1,2] In this context, bi-magnetic core|shell (CS) nanoparticles (NPs) have attracted considerable interest over the last decades, due to the many intriguing phenomena stemming from the coupling at the interface.[3,4] Frequently, the exchange interaction between two different magnetically ordered phases gives rise to exchange bias (H_E), that consists in a horizontal hysteresis loop shift and a coercive field (H_C) increase, after cooling the sample in a magnetic field.[5] This behavior originates from the pinning force exerted by the antiferromagnetic (AFM) phase, which leads to a dominant unidirectional anisotropy.[6] This unidirectional anisotropy makes the switching of the magnetization of the ferromagnetic one (FM) more difficult in the direction opposite to the cooling field.

Since his discovery, exchange bias has been proposed as an efficient tool for several applications, including the enhancement of the performances of permanent magnets.[7,8] However, scientific community has never felt the urgency to develop this idea, mostly because of the difficulties in building up complex heterostructures and to the large availability of Rare Earth (RE) permanent magnets.[3,9] The criticality of RE-elements, emerged in the last few years, [10] is pushing researchers to find feasible alternative approach to

develop novel RE-free materials. In addition, the tremendous improvement in controlling the quality of heterostructures at the nanoscale makes nowadays the exploitation of the exchange bias a promising and feasible strategy to attempt to solve the problem of RE-based permanent magnets.[11]

Being a boundary effect, H_E is critically influenced by the quality of the interface shared by the two phases, and it is promoted by an epitaxial relationship.[12,13] Because of the similarity in packing of the oxygen ions, spinel and rock-salt phases are useful building blocks to produce high-quality epitaxial superlattices.[14] Accordingly, several transition metal oxides with these crystal structures have been exploited to realize exchange coupled CS NPs, the inverted AFM|ferrimagnetic (AFM|FiM) $Fe_xO|Fe_3O_4$, CS system being the most investigated.[15–18]

A major issue of the $Fe_xO|Fe_3O_4$ exchange coupled nanosystem in view of a possible application as permanent magnet is the low magnetic anisotropy of the ferromagnetic layer. This limitation can be overcome by simply doping the spinel ferrite with a certain amount of Co^{2+} ions.[19] On the other hand, doping the spinel ferrite with cobalt, offers the additional advantage of increasing the low ordering temperature of Fe_xO (Fe_xO T_N = 205 K, CoO T_N = 298 K).

Here we report on the investigation of exchange bias properties in a family of $Co_xFe_{1-x}O|Co_xFe_{3-x}O_4$ CS NPs obtained through one-pot thermal decomposition of mixed cobalt and iron oleate complexes. We show how the high crystalline quality of the AFM material and its boundary with FiM shell without cationic intermixing lead to exceedingly high H_E, even in systems where both components exhibit high magnetic anisotropy, a phenomenon which has never been previously reported for CS NPs.[20] On the other hand, the possibility of engineering CS NPs where the size of the AFM core could be systematically varied, while the

others structural parameters remained unchanged, allowed us to address its effect on the exchange coupling in this class of materials. In particular, we identified the minimum amount of the AFM phase which maximizes the energy product of the exchange coupled system and thus the performances as permanent magnet.

RESULTS AND DISCUSSION

CS NPs based on a $Co_xFe_{1-x}O$ core and $Co_xFe_{3-x}O_4$ shell were synthesized by one-pot thermal decomposition of $(Co^{2+}Fe^{3+})$-oleate, following a procedure slightly modified from the one by Park *et al.*[21] (see Supporting Information). Transmission Electron Microscopy (TEM) images, reported in Figure 1a, show a spherical shape and unique size population for all NPs. The corresponding particle size histograms, displayed in the insets, are consistent with a Gaussian distribution with a narrow particle size distribution (≤ 15%) and mean diameter of 6(1), 9(1), 15(2) and 18(1) nm. In the following the samples will be denotes as CS#, where # corresponds to the mean diameter. The control of the average particle size was achieved by varying the decomposition temperature; specifically, by setting the temperature at 300, 315, 335 and 350 °C, NPs with progressively larger average size were obtained. The increase of the particle size with the decomposition temperature is indeed expected, due to the increased reactivity of the metal-oleate precursor.[21–23] Interestingly, in our case, such dependence follows a linear behavior, as shown in Figure S1, Supporting Information.

High-Angle Annular Dark-Field (HAADF) images demonstrate the formation of a CS structure: Figure 1b clearly shows two different regions in the NP, an inner core with higher contrast and an outer shell with lower contrast. In order to corroborate the formation of a CS structure the local fast Fourier transform (FFT) of a HAADF image and their respective inverse FFT were analyzed. FFT images acquired from core and shell regions, revealed the

presence of similar face-centered cubic structures (see Figure S2, Supporting Information): the core region has the typical periodicity of the rock-salt phase ($Co_xFe_{1-x}O$), while the shell shows extra diffraction spots related to the cubic spinel structure ($Co_xFe_{3-x}O_4$), as the 0.30 nm interplanar distance between (220) planes. Interestingly, from the inverse FFT obtained by selecting the spinel (220) reflections (Figure S2, Supporting Information), the corresponding planes are clearly visible mainly in the outer part of the NP, as expected for a CS architecture.

Electron-Energy-Loss Spectroscopy (EELS) analysis was performed in order to assess the elemental distribution within the NPs (see Figures 2a and S3). Elemental quantification shows a clear CS structure with a non-homogeneous distribution of iron, cobalt and oxygen along the NP diameter. Curiously, even if for each sample the ion distributions change with radial distance, the stoichiometry of the core and shell regions are the same for all the investigated samples, independently of the particle size. The stoichiometry of the two regions was evaluated by analyzing the oxygen-to-metal ratio variation, shown in Figure 2b. A sharp change from ~1.0 to ~1.3 occurs at a given radial distance for each sample, confirming the $MO|M_3O_4$ CS stoichiometry. Since these compounds are characterized by the presence of only divalent ions in the MO core, and by a combination of divalent and trivalent ions in the M_3O_4 shell, a variation in the cobalt-to-iron ratio should be expected in order to maintain charge neutrality (as discussed below, we can reasonably assume that only iron ions are in the trivalent state). In fact, as reported in Figure 2b, while the iron content is mainly constant along the NP, cobalt is present in a higher amount into the inner region than in the outer one, the cobalt-to-iron ratio varying from ~0.43 in the core to ~0.25 in the shell. Furthermore, the Fe^{2+} and Fe^{3+} distribution in the NP was examined. EEL mapping, obtained by fitting reference spectra to the acquired spectrum image and shown in Figure 2c, displays an evident segregation of iron ions with different oxidation states: Fe^{2+} ions are mostly confined in the core region, while Fe^{3+} ions are exclusively located in the shell. These data demonstrate that

the oxidation process is associated to a Co^{2+} self-diffusion ion mechanism, where the NPs release the excess of cobalt atoms to the solution media in order to allow the formation of the spinel shell.[24] Combining all these results, core and shell structures can be finally assigned to rock-salt $Co_{0.3}Fe_{0.7}O$ and spinel $Co_{0.6}Fe_{2.4}O_4$ stoichiometries. Comparing different samples, it emerges that NPs have a different average core diameter, which increases with the total particle size, while the shell thickness remains roughly constant (~2 nm), independently of particle size, reaction temperature or solvent.

X-Ray Diffraction (XRD) analysis (Figure S4, Supporting Information) confirms the presence of two crystallographic phases, which can be indexed as face-centered cubic rock-salt and cubic spinel phase; the structural parameters obtained from the Rietveld refinement are reported in Table 1. Interestingly, in larger NPs (CS15 and CS18) the cell parameter of the rock-salt phase falls in between those expected for cobalt and iron monoxide (0.425 and 0.429 nm for CoO and FeO, respectively), confirming the formation of a mixed cobalt and iron monoxide.[25–27] Conversely, when the core particle size decreases, the rock-salt unit cell undergoes to a progressive contraction. On the other hand, the spinel phase presents a similar but opposite behavior: the cell parameter of CS15 and CS18 corresponds to that expected for $Co_{0.6}Fe_{2.4}O_4$,[28] while a slight expansion is observed on decreasing the particle size. It has to be stressed that the deviation of the cell parameter from the bulk value, in our case, is not related to interface effects, as it is observed in epitaxial films where the cell parameter tends to the value of the substrate when the film becomes thinner.[29] On the contrary, in our case both the contraction and expansion of the cell parameters arise from the shell pressure over the core, and *vice versa*, are considered as a manifestation of coherent interface between the two phases. A similar behavior has indeed been previously observed in $Fe_xO|Fe_3O_4$ CS NPs.[14,18,30] In addition, it should be stressed that interphase mismatch between core and shell grows from small to large NPs, (from 0.2% for CS6 to 1.4% for CS18). This increase can be

related to the loss of contraction or expansion suffered by the core or the shell in extremely confined system like small NPs. Crystal sizes obtained from profile broadening analysis for rock-salt and spinel phases are also reported in Table 1. Due to the broadness of the diffraction peaks of the spinel structure and to the overlap between the peaks of the two phases, the following procedure was adopted: starting from the mean diameter values obtained from TEM image statistics, core diameter (d_C) and shell thickness (t_S) were estimated considering a solid sphere shape and a spherical crown, respectively, with volume ratio equal to that obtained from Rietveld evaluation.[31,32] With these assumptions we obtained that the as-synthesized NPs have a constant shell thickness of ~1.4 nm and a core diameter which increases from 3.2 to 14.8 nm (see Table 1), in agreement with EELS results.

To conclude, the structural characterization (XRD, HAADF) denotes each sample has rock-salt|spinel CS architecture. In particular, also considering the EELS results, the formation of a series of $Co_{0.3}Fe_{0.7}O|Co_{0.6}Fe_{2.4}O_4$ CS NPs with variable core diameter and constant shell thickness of ~2 nm is evidenced. The formation of AFM|FiM CS nanostructures by thermal decomposition of Fe^{3+}-oleate was previously reported in the literature.[14,15] Indeed, it has been shown that Fe^{3+}-oleate decomposition at high temperatures allows the formation of $Fe_xO|Fe_3O_4$ CS NPs through the initial reduction of Fe^{3+} ions to Fe^{2+} due to the breakup of the oleate chain, forming Fe_xO NPs. Later, the surface oxidation of Fe_xO during purification and separation processes leads to the formation of a Fe_3O_4 shell.[33] However, $Fe_xO|Fe_3O_4$ CS NPs obtained from Fe^{3+}-oleate undergo a progressive oxidation and thus to the thickening of the Fe_3O_4 shell till the complete disappearance of the AFM core.[34] Conversely, as it can be seen in Figure S5 Supporting Information, the CS NPs structure does not change with the aging of the samples, probably thanks to the higher stability of Co^{2+} ions with respect to Fe^{2+} ones ($E^0_{Fe(III)/Fe(II)}$ = 0.77 V and $E^0_{Co(III)/Co(II)}$ = 1.82 V).[35] Finally, it should be noted that the close relationships between cell parameters of both phases (cell mismatch less than 2%)

suggests that the spinel shell formation occurs by a topotaxial transformation of the particle surface through the oxidation of initial $Co_{0.3}Fe_{0.7}O$. Notably, this mechanism allows for the formation of a sharp boundary between the two phases. HAADF simulation images at [100] and [011] directions corroborate the good matching between the core and the shell observed in the experimental images (see Figures 1b and S6).[36] Interestingly, even for smaller NPs, (CS6) where the reduction in size was found to induce structural distortions, (cell expansion and contraction of the spinel shell and rock-salt core, respectively), the good matching between the two phases was preserved.[14,30]

From the point of view of the magnetic properties, $Co_{0.3}Fe_{0.7}O|Co_{0.6}Fe_{2.4}O_4$ CS NPs can be considered as a single inverted exchange biased CS system, where the AFM phase is placed in the core and the FiM one in the shell, and the ordering temperature of the AFM phase, $T_N(Co_{0.30}Fe_{0.7}O)$, expected between 198 and 291 K, is lower than that of the FiM one, $T_C(Co_{0.6}Fe_{2.4}O_4) = 820$ K.[37,38] Interestingly, the series of CS NPs shows some characteristics which make it an ideal candidate to systematically address the effect of the size of AFM counterpart on the final magnetic properties of the nanosystem.[39,31] This effect has been much less investigated than the influence of the FM size.[4] All the samples, indeed exhibit the same morphology (narrow particle size distribution, spherical shape and constant 2 nm FiM shell thickness), a sharp interface and a high quality structural matching.

At first, the temperature dependence of the magnetization after zero-field cooling (ZFC) and field cooling (FC) processes was measured (Figure 3a). For all CS NPs the ZFC curves present a maximum at different temperatures, T_1, above which magnetization decays monotonically and merges with the FC curve. T_1 is size dependent (see Table 2) and increases with particle size. In particular, it scales with the volume of the FiM phase (see Figure S7, Supporting Information). This behavior is characteristic of superparamagnetic

systems, and then, T_1 can be associated to the blocking temperature (T_B) of the FiM spinel shell phase ($Co_{0.6}Fe_{2.4}O_4$), being, as a first approximation, $T_B = KV/25k_B$ (K is the effective anisotropy constant, V is the FiM volume and k_B is the Boltzmann's constant).[40] Larger NPs (CS18) are still blocked at RT, as expected for cobalt ferrite NPs of 14 nm which is the equivalent particle size of a sphere with the same volume of a crown sphere of 14 and 18 nm internal and external radius, respectively.[28] Furthermore, it should be noted that in the FC curves of CS15 and CS18 another maximum in magnetization (T_2) is observed at a fixed temperature $T_2 \approx 220$ K. A similar increase in the magnetization is also visible in the ZFC curves, even if the kink becomes less prominent as particles size decreases. In order to elucidate the nature of the observed magnetic transitions, 30 kOe FC magnetization *vs.* temperature curves were acquired (see Figure 3b). With the exception of the smallest NPs (CS6), where AFM rock-salt phase is present only in small amount, at 30 kOe the FC curves always present a maximum in magnetization at 220 K. This temperature can be attributed to the T_N of the AFM rock-salt core phase. Notably, this value is intermediate between the T_N of bulk FeO and CoO (198 and 291 K, respectively).[5,41] As reported in the literature, indeed, there exists a linear dependence of T_N with cobalt amount in Co-doped wüstite, being FeO and CoO isostructural antiferromagnetic oxides.[42,43] The estimation of T_N for a $Co_{0.3}Fe_{0.7}O$ structure, assuming the linear dependence,[44] provides $T_N = 226$ K, that is very close to the experimental one. It deserves to be stressed that we observed T_N even for very low size of the AFM phase (5 nm). This result is rather surprising, since for FeO the appearance of the Néel transition is usually reported only for much larger NPs size[18] and it can be probably ascribed to the large magnetocrystalline anisotropy of the mixed monoxide, which makes the material less prone to size effects.[45] Moreover, for the smallest CS NPs we cannot exclude that T_N is not visible just because of the too low contribution of the AFM phase or for a progressive loss of magnetic order.

Figure 4 depicts ZFC hysteresis loops recorded at 10 K, normalized by the magnetization at 120 kOe. ZFC loops show large H_C, in agreement with those expected for cobalt ferrite NPs with similar stoichiometry.[28] In particular, H_C^{ZFC} values are almost constant around 13 kOe, with only a small decrease (< 10%) on passing from small to large particle size. The observed behavior, which is markedly different from that commonly observed in single phase magnetic NPs,[28,46] may arise from a combination of size and morphological effects: in fact, the ZFC behavior is mainly determined by the FiM shell, which is characterized by a large surface-to-volume ratio because of its geometry. Moreover, due to the small shell thickness, we cannot exclude that non-coherent magnetization reversal processes are operating, depending on the curvature of inner and outer surfaces. The ZFC hysteresis loops are well far from the saturation regime even at high fields, although the reversibility regime was reached close to the highest measuring field and no vertical shifts were observed.[47] The non-saturation behavior can be explained by the presence of a high anisotropic AFM material.

In order to study the exchange coupling properties, low temperature hysteresis loops were measured after FC from RT in a 120 kOe field. The loops show the presence of H_E, i.e. a loop-shift along the field axis, and an enhancement in H_C^{FC}, denoting an increase in the effective magnetic anisotropy of the system. These features are typical for exchange coupled AFM and FM or FiM materials.[6] Interestingly, we did not observe any vertical shift of the loops, as reported in previous works focused on similar AFM|FiM CS NPs.[35,48,49] In these cases the shift was attributed to the role of uncompensated spins in the FiM layer. However, we believe this effect should be rather related to the fact that the maximum applied field was not large enough to reach the fully reversible regime, independently of any field cooling procedure.[31,47] The validity of this description is well demonstrated by the FC minor loop recorded only up to 70 kOe on CS9 (see Fig. S8): unlike the full loop, the minor cycle is largely shifted along the vertical axis.

An extremely large H_E values, with a maximum of 8.6 kOe for 9 nm CS9 NPs is observed in the FC hysteresis loops. To our knowledge, this corresponds to one of the largest H_E ever reported for CS NPs. This large value can be attributed to the high crystallinity and magnetic anisotropy of the AFM counterpart and to the high quality of the interface with the FiM shell, i.e. the excellent matching of the two lattices and the remarkable sharp interface.[4,36] Interestingly, the high magnetic anisotropy of both the core and shell regions should theoretically quench H_E and produce the increase of the coercive field alone.[20,50,51] Conversely, in this system we observed simultaneously both phenomena. Indeed, while the demagnetizing branches are shifted towards larger fields, the magnetizing ones are perfectly superimposed with those of the ZFC loops, pointing out that the enhancements of H_C are related to the presence of H_E. Therefore, we can conclude that classical macroscopic H_E theories are not fully valid for CS NPs,[3,4,52] and more sophisticated theories such as perpendicular coupling must be considered.[4,53] Interestingly, previous results on highly anisotropic CS NPs have revealed different types of exchange coupling behavior. If in some cases no H_E was observed and this was ascribed to the high anisotropy of both counterparts,[50,51,54] in some others moderate and large H_E values were reported, although the anisotropy of the materials involved was similarly large.[48,49] However, in our opinion, a high-quality structural matching between core and shell regions their sharp interface and the well-defined crystallographic structure of the AFM materials are crucial issues to realize excellent exchange-coupled materials. Another remarkable effect of exchange bias is that of largely increasing the area of the hysteresis loop. Since the loop area corresponds to the energy losses in a full cycle and hence to the magnetic energy stored in the material[55] we can argue that this effect can be a powerful tool on the way of building up RE-free permanent magnets (see discussion below).

The temperature dependence of FC hysteresis loops, measured for CS18, (see Figure S9, Supporting Information) further elucidated the nature of the observed magnetic transitions (T_1 and T_2). Both H_C^{FC} and H_E display a dramatic reduction as the temperature increases. In particular, while H_C^{FC} approaches zero at RT, H_E vanishes at 210 K. This behavior is in good agreement with the description given above: H_C^{FC} disappears close to the observed T_B when the FiM spinel shell becomes superparamagnetic; conversely, H_E vanishes above the ordering temperature of the AFM-core, confirming indirectly the interpretation of T_2 as T_N of the AFM-core region.[4]

The present series of AFM|FiM CS NPs is an ideal candidate for a systematic analysis of the dependence of exchange-coupling effect on the size of the AFM core. In Figure 5 the dependencies of H_C and H_E as a function of the AFM-core diameter (d_{AFM}) are shown. Interestingly, both parameters show non-monotonic trend with d_{AFM}, as they exhibit a maximum for CS9 (d_{AFM} = 5 nm) and a subsequent decay to a value that remains constant for the two larger samples (CS15 and CS18). Regarding H_E, its dependence is in good agreement with that theoretically predicted[4,56] and experimentally observed[4,57,58] in AFM|FM bilayers. The non-monotonic dependence is described by considering the concomitant effect of the energy barrier of the AFM material ($K_{AFM}V_{AFM}$) and the formation and growth of AFM domains, which are responsible for the onset and the maximum of H_E, respectively.[31,56] However, due to the reduced volume of our CS NPs, the formation and growth of AFM domains appears rather unlikely. An alternative explanation, recently proposed after some MonteCarlo simulations, suggests the competition between uncompensated spins of the core and shell regions as responsible of the H_E size dependence in AFM|FiM CS NPs.[59] Uncompensated spins, which comes mainly from the non-collinearity of the two AFM and FiM sublattices[60,61] and from structural defects,[62] have been demonstrated to be related to the exchange bias phenomena.[63] The non-monotonic dependence, thus, can be better attributed to

a crossover in the relative number of uncompensated spins located in the FiM surface, i.e. the outer surface of the NPs, or in the AFM-core and FiM-shell interface.

Also the H_C^{FC} dependence has been previously interpreted in terms of domain formation in highly anisotropic AFM materials[57] or of competition of uncompensated spins in the CS structure.[59] In our case, however, the maxima of H_C^{FC} and H_E occurs at similar d_{AFM}. This behavior, which is different from that reported in the literature for other exchange coupled systems, where the maximum of H_C^{FC} is usually reached at lower size than H_E, clearly demonstrates that the increase of coercivity is driven by the presence of the induced bias in the demagnetizing branches of the loop. Therefore, the standard models which predict different trends for coercivity and exchange bias do not fully describe the behavior of AFM|FiM CS NPs with high anisotropy of both components.

The evolution of the magnetic properties with the size of the AFM core provides precious information about the optimal relative amount of AFM and FiM (or ferromagnetic) phases to be combined to design an exchange-coupled permanent magnet. The performance of a material as permanent magnet is normally quantified by the so-called maximum energy product, BH_{max}, which is defined as twice the maximum magnetostatic energy available from a magnet of optimal shape.[55] In our case, the relative increase of BH_{max} before and after the FC procedure, $BH_{max}^{FC}/BH_{max}^{ZFC}$, has the same non-monotonous trend observed for H_C and H_E ($BH_{max}^{FC}/BH_{max}^{ZFC}$ = 2, 7, 3, 1 for CS6, CS9, CS15 and CS18, respectively), confirming the strong effect of bias on the permanent magnet properties. More interestingly, we observed a very large increase of BH_{max} (more than 7 times for CS9), for a relatively low amount of AFM phase (ca. 20% in volume). Given the very low magnetization of AFM nanomaterials,[64,65] this aspect assumes a crucial relevance to preserve a high magnetic flux in the composite. Indeed, a large volume of the AFM phase could significantly affect M_S compromising $(BH)_{max}$.[7,8]

CONCLUSIONS

In summary, a series of narrowly size distributed $Co_{0.3}Fe_{0.7}O$(AFM)|$Co_{0.6}Fe_{2.4}O_4$(FiM) CS NPs with mean diameter from 6 nm to 18 nm was synthesized through the one-pot thermal decomposition of a (Co^{2+},Fe^{3+})-oleate precursor. The formation of the CS structure was obtained by topotaxial oxidation of the core region leading to a series of CS NPs with variable AFM-core size and constant FiM-shell thickness. The excellent interphase matching and the well-defined CS morphology and stoichiometry for all the series makes it a proper candidate for a systematic analysis of the exchange-coupling dependence on the AFM size in AFM|FiM CS NPs. Accordingly, magnetic characterization has revealed ZFC hysteresis loops with large irreversible fields and H_C almost independent of particle size. In addition, upon field cooling the robust exchange-coupling between AFM and FiM phases was demonstrated to give rise to one of the largest value of H_E ever reported for CS NPs (8.6 kOe) and to an enhanced H_C. The combination of these two effects leads to a significant increase of the energy stored in the material, even in a highly anisotropic material such as cobalt ferrite nanoparticles and for a relatively low amount of AFM phase. Therefore, biasing is demonstrated to be a powerful strategy to improve the performance of RE- free permanent magnets, which is currently a largely investigated research area. Although the low ordering temperatures of the most common high anisotropy AFM components may appear a critical limitation to the proposed approach, it should be observed that the combination of magnetic proximity effects[66,67] and high susceptibility AFM materials[68] can enhance the effectiveness of exchange bias at higher temperatures, suitable for practical applications.

Interestingly, the FC process was found to affect the loop on the demagnetizing branches only, suggesting that classical macroscopic H_E theories do not accurately describes the

behavior of high anisotropic CS NPs. Both H_C^{FC} and H_E depict a non-monotonic trend with d_{AFM}, showing a maximum value at d_{AFM} = 5 nm. The observed trend for H_E was explained by the internal competition between uncompensated spins at the NP surface and core-shell interface.

MATERIALS AND METHODS

The synthesis was carried out using standard airless procedures and commercially available reagents: 1-octadecene (ODE, 90%), docosane (DCE, 99%), ethanol (EtOH, >99.8%), hexane (Hx, >95%), oleic acid (OA, 90%), sodium oleate (NaOl, >97.0%), iron(III) chloride hexahydrate ($FeCl_3 \cdot 6H_2O$, >98%), cobalt(II) chloride hexahydrate ($CoCl_2 \cdot 6H_2O$, >98%). All starting materials were purchased from Sigma-Aldrich, except sodium oleate that was acquired from TCI America, and used without further purification.

Monodisperse spherical NPs were synthesized through thermal decomposition of metal-oleate complex in high-boiling solvent containing oleic acid as stabilizing surfactant, following a procedure slightly modified from that developed by Park et al.[21] The metal-oleate complexes were prepared dissolving 4 mmol of $FeCl_3 \cdot 6H_2O$, 2 mmol of $CoCl_2 \cdot 6H_2O$ and 16 mmol of NaOl in 10 mL of H_2O, 10 mL of ethanol and 20 mL of hexane and heating the mixture to reflux for 4 h. In a typical synthesis, 1.5 g of mixed metal-oleate complex ($(Co^{2+}Fe^{3+})$-oleate) and 0.15 g of OA were dissolved in 10 g of ODE or DCE in a 50 mL three-neck round bottom flask. The mixture was heated to the desired decomposition temperature at 3 °C min^{-1} for 2 h. Four different decomposition temperatures were selected, 300, 315, 335 and 350 °C, leading to the formation of NPs of different size. Finally, the flask was removed from the heating mantle and allowed cooling down. During heating, digestion and cooling processes the mixture was exposed to an N_2 flow. All NPs were washed by

several cycles of coagulation with ethanol, centrifugation at 5000 rpm, disposal of supernatant solution and re-dispersion in hexane.

Transmission electron microscopy (TEM) images were obtained using a CM12 Philips microscope with a LaB_6 filament operated at 100 kV. High resolution high angle annular dark field images (HAADF) were acquired on a FEI Titan 'cubed' microscope equipped with a probe corrector (probe size 0.08 nm, convergence 22 mrad, inner detector angle 50 mrad) operated at 300 kV. High resolution images (HR-TEM) were acquired on a JEOL JEM-2200FS operated at 200 keV, setting the spherical aberration to a small negative value (~ -30 μm) to obtain a low delocalization and a high phase contrast transfer at high frequencies, and by filtering the elastic signal with the Ω-filter to further increase contrast. The electron energy loss (EEL) profiles for the particles with different sizes were acquired on the same instrument with the filter in spectroscopy mode. The quantification of O-K, Fe-$L_{2,3}$, and Co-$L_{2,3}$ edges was performed using EELSMODEL and a Likelihood derived fitter algorithm for Poisson statistics, to assure the highest possible accuracy and precision.[69] High resolution EEL maps to determine the Fe valence were obtained at 120 kV with a Gatan Enfinium SR spectrometer and by exciting the monochromator, to reach an energy resolution of ~0.25 eV in the Fe-$L_{2,3}$ edge. Fe^{2+} and Fe^{3+} maps were obtained by fitting reference spectra to the acquired spectrum image. The simulations of the core/shell structure and the EEL profiles were done assuming a perfect match between rock-salt core and cubic spinel shell, and a full occupancy at the atomic sites. Simulated HAADF images of the core/shell particles were obtained with STEM_CELL using a linear approximation,[70] taking into account the detector collecting angle (50 mrad – 180 mrad) and the nominal probe size (0.08 nm). The NPs were dispersed in hexane and then placed dropwise onto a carbon supported grid. The particles size and the standard deviation were obtained by calculating the number average by manually measuring the diameters of more than 300 particles from TEM images.

The determination of cobalt and iron concentration in the sample was performed using a Rigaku ZSX Primus II X-ray fluorescence spectrometer (XRF). The structure of the NPs was investigated by X-ray powder diffraction (XRD) using a Bruker New D8 ADVANCE ECO diffractometer with a Cu Kα radiation. The measurements were carried out in the range 25-70°, with a step size of 0.03° and a collection time of 1.5 s. Quantitative analysis of the XRD data was performed with a full pattern fitting procedure based on the fundamental parameter approach (Rietveld method)[71] using the Topas 2.0 software package (Bruker AXS).

The magnetic properties of the NPs were measured on tightly packed powdered samples using a vibrating sample mode magnetometer with 120 kOe (MagLab VSM12T-Oxford) and 90 kOe (VSM, Quantum Design PPMS) maximum field. Magnetization versus temperature measurements were performed in zero-field cooled (ZFC) and field cooled (FC) conditions with 50 Oe or 30 kOe probe fields. Hysteresis loops were measured in ZFC and FC conditions after cooling from RT to 10 K with a 120 kOe applied field.

ASSOCIATED CONTENT

Supporting Information.

Dependence of the CS NPs size on the decomposition temperature of $(Co^{2+}Fe^{3+})$-oleate precursor. Indexed HR-TEM FFT for core and shell regions and inverted FFT image from the (220) diffraction spots. Simulated HAADF images for the rock-salt and spinel structures and superposition of the two. Experimental and simulated EELS profiles. XRD patterns. Dependence of T_B and T_N on the volume of the FiM phase. FC hysteresis loops of CS9 recorded at 10 K in the ± 70 kOe and ± 120 kOe field ranges, and of CS18 recorded at increasing temperatures, from 10 K to 300 K. Temperature dependence of H_C and H_E for

CS18. Room temperature hysteresis loops. This material is available free of charge *via* the Internet at http://pubs.acs.org.

AUTHOR INFORMATION

Corresponding Author

*E-mail: lopezortega.alberto@gmail.com; csangregorio@iccom.cnr.it

Author Contributions

EL, ALO, CJF and CS conceived the idea. EL and ALO synthesized the nanoparticles and performed the measurements. GB, ST, MM, GVT and GS performed electron microscopy measurements. EL, ALO, CJF and CS wrote the manuscript. All authors contributed to revise the manuscript.

Note

The authors declare no competing financial interest.

ACKNOWLEDGMENTS

This work was supported by the EU-FP7 through NANOPYME Project (No. 310516) and Integrated Infrastructure Initiative ESTEEM2 (No. 312483). S.T. gratefully acknowledges the FWO Flanders for a post-doctoral scholarship.

REFERENCES:

(1) Skumryev, V.; Stoyanov, S.; Zhang, Y.; Hadjipanayis, G.; Givord, D.; Nogués, J. Beating the Superparamagnetic Limit with Exchange Bias. *Nature* **2003**, *423*, 850–853.

(2) López-Ortega, A.; Estrader, M.; Salazar-Alvarez, G.; Roca, A. G.; Nogués, J. Applications of Exchange Coupled Bi-Magnetic Hard/soft and Soft/hard Magnetic Core/shell Nanoparticles. *Phys. Rep.* **2015**, *553*, 1–32.

(3) Meiklejohn, W. H.; Bean, C. P. New Magnetic Anisotropy. *Phys. Rev.* **1956**, *102*, 1413–1414.

(4) Nogués, J.; Sort, J.; Langlais, V.; Skumryev, V.; Suriñach, S.; Muñoz, J. S.; Baró, M. D. Exchange Bias in Nanostructures. *Phys. Rep.* **2005**, *422*, 65–117.

(5) Berkowitz, A. E.; Takano, K. Exchange Anisotropy — a Review. *J. Magn. Magn. Mater.* **1999**, *200*, 552–570.

(6) Nogués, J.; Schuller, I. K. Exchange Bias. *J. Magn. Magn. Mater.* **1999**, *192*, 203–232.

(7) Sort, J.; Nogués, J.; Suriñach, S.; Muñoz, J. S.; Baró, M. D.; Chappel, E.; Dupont, F.; Chouteau, G. Coercivity and Squareness Enhancement in Ball-Milled Hard Magnetic–antiferromagnetic Composites. *Appl. Phys. Lett.* **2001**, *79*, 1142.

(8) Sort, J.; Suriñach, S.; Muñoz, J. S.; Baró, M. D.; Nogués, J.; Chouteau, G.; Skumryev, V.; Hadjipanayis, G. C. Improving the Energy Product of Hard Magnetic Materials. *Phys. Rev. B* **2002**, *65*, 174420.

(9) Jimenez-Villacorta, F.; Lewis, L. H. Advanced Permanent Magnetic Materials. In *Nanomagnetism*; Gonzalez Estevez, J. M., Ed.; One Central Press, 2014; pp. 160–189.

(10) Critical Raw Materials http://ec.europa.eu/growth/sectors/raw-materials/specific-interest/critical/index_en.htm.

(11) Gutfleisch, O.; Willard, M. a; Brück, E.; Chen, C. H.; Sankar, S. G.; Liu, J. P. Magnetic Materials and Devices for the 21st Century: Stronger, Lighter, and More Energy Efficient. *Adv. Mater.* **2011**, *23*, 821–842.

(12) Evans, R. F. L.; Bate, D.; Chantrell, R. W.; Yanes, R.; Chubykalo-Fesenko, O. Influence of Interfacial Roughness on Exchange Bias in Core-Shell Nanoparticles. *Phys. Rev. B* **2011**, *84*, 092404.

(13) Leighton, C.; Nogués, J.; Jönsson-Åkerman, B. J.; Schuller, I. K. Coercivity Enhancement in Exchange Biased Systems Driven by Interfacial Magnetic Frustration. *Phys. Rev. Lett.* **2000**, *84*, 3466–3469.

(14) Wetterskog, E.; Tai, C. W.; Grins, J.; Bergström, L.; Salazar-Alvarez, G. Anomalous Magnetic Properties of Nanoparticles Arising from Defect Structures: Topotaxial Oxidation of Fe(1-x)O|Fe(3-δ)O4 Core|shell Nanocubes to Single-Phase Particles. *ACS Nano* **2013**, *7*, 7132–7144.

(15) Sun, X.; Huls, N. F.; Sigdel, A.; Sun, S. Tuning Exchange Bias in Core/shell FeO/Fe3O4 Nanoparticles. *Nano Lett.* **2012**, *12*, 246–251.

(16) Lak, A.; Kraken, M.; Ludwig, F.; Kornowski, A.; Eberbeck, D.; Sievers, S.; Litterst, F. J.; Weller, H.; Schilling, M. Size Dependent Structural and Magnetic Properties of

FeO-Fe3O4 Nanoparticles. *Nanoscale* **2013**, *5*, 12286–12295.

(17) Khurshid, H.; Chandra, S.; Li, W.; Phan, M. H.; Hadjipanayis, G. C.; Mukherjee, P.; Srikanth, H. Synthesis and Magnetic Properties of Core/shell FeO/Fe3O4 Nano-Octopods. *J. Appl. Phys.* **2013**, *113*, 17B508.

(18) Estrader, M.; López-Ortega, A.; Golosovsky, I. V; Estradé, S.; Roca, A. G.; Salazar-Alvarez, G.; López-Conesa, L.; Tobia, D.; Winkler, E.; Ardisson, J. D.; *et al.* Origin of the Large Dispersion of Magnetic Properties in Nanostructured Oxides: Fe(x)O/Fe3O4 Nanoparticles as a Case Study. *Nanoscale* **2015**, *7*, 3002–3015.

(19) Fantechi, E.; Campo, G.; Carta, D.; Corrias, A.; de Julián Fernández, C.; Gatteschi, D.; Innocenti, C.; Pineider, F.; Rugi, F.; Sangregorio, C. Exploring the Effect of Co Doping in Fine Maghemite Nanoparticles. *J. Phys. Chem. C* **2012**, *116*, 8261–8270.

(20) Lavorato, G. C.; Lima, E.; Tobia, D.; Fiorani, D.; Troiani, H. E.; Zysler, R. D.; Winkler, E. L. Size Effects in Bimagnetic CoO/CoFe2O4 Core/shell Nanoparticles. *Nanotechnology* **2014**, *25*, 355704.

(21) Park, J.; An, K.; Hwang, Y.; Park, J.-G.; Noh, H.-J.; Kim, J.-Y.; Park, J.-H.; Hwang, N.-M.; Hyeon, T. Ultra-Large-Scale Syntheses of Monodisperse Nanocrystals. *Nat. Mater.* **2004**, *3*, 891–895.

(22) Bao, N.; Shen, L.; An, W.; Padhan, P.; Heath Turner, C.; Gupta, A. Formation Mechanism and Shape Control of Monodisperse Magnetic CoFe 2 O 4 Nanocrystals. *Chem. Mater.* **2009**, *21*, 3458–3468.

(23) Chen, R.; Christiansen, M. G.; Anikeeva, P. Maximizing Hysteretic Losses in Magnetic Ferrite Nanoparticles via Model-Driven Synthesis and Materials Optimization. *ACS Nano* **2013**, *7*, 8990–9000.

(24) Lottini, E. Magnetic Nanostructures: A Promising Approach towards RE-Free Permanent Magnets, PhD Thesis University of Florence, 2016.

(25) Denton, A. R. and Ashcroft, N. W. Vegard's Law. *Phys. Rev. A* **1991**, *43*, 3161–3164.

(26) Pongsai, S. B. Computational Study on Thermodynamics of Mixing and Phase Behaviour for CoO/FeO and CoO/MnO Solid Solutions. *J. Mol. Struct.* **2006**, *761*, 171–175.

(27) Clendenen, R. L. Lattice Parameters of Nine Oxides and Sulfides as a Function of Pressure. *J. Chem. Phys* **1966**, *44*, 4223-4228.

(28) López-Ortega, A.; Lottini, E.; Fernández, C. D. J.; Sangregorio, C. Exploring the Magnetic Properties of Cobalt-Ferrite Nanoparticles for the Development of a Rare-Earth-Free Permanent Magnet. *Chem. Mater.* **2015**, *27*, 4048–4056.

(29) Bean, J. C.; Feldman, L. C.; Fiory, A. T.; Nakahara, S.; Robinson1, I. K. GexSi1−x/Si Strained-Layer Superlattice Grown by Molecular Beam Epitaxy. *J. Vac. Sci. Techno. A* **1984**, *2*, 436-440.

(30) Pichon, B. B. P. B.; Gerber, O.; Lefevre, C.; Florea, I.; Fleutot, S.; Baaziz, W.; Pauly, M.; Ohlmann, M.; Ulhaq, C.; Ersen, O.; *et al.* Microstructural and Magnetic Investigations of Wüstite-Spinel Core-Shell Cubic-Shaped Nanoparticles. *Chem. Mater.* **2011**, *23*, 2886–2900.

(31) Salazar-Alvarez, G.; Sort, J.; Suriñach, S.; Baró, M. D.; Nogués, J. Synthesis and Size-

Dependent Exchange Bias in Inverted Core-Shell MnO|Mn3O4 Nanoparticles. *J. Amer. Chem. Soc.* **2007**, *129*, 9102–9108.

(32) López-Ortega, A.; Tobia, D.; Winkler, E.; Golosovsky, I. V; Salazar-Alvarez, G.; Estradé, S.; Estrader, M.; Sort, J.; González, M. A.; Suriñach, S.; *et al.* Size-Dependent Passivation Shell and Magnetic Properties in Antiferromagnetic/ferrimagnetic Core/shell MnO Nanoparticles. *J. Am. Chem. Soc.* **2010**, *132*, 9398–9407.

(33) Hai, H. T.; Yang, H. T.; Kura, H.; Hasegawa, D.; Ogata, Y.; Takahashi, M.; Ogawa, T. Size Control and Characterization of Wustite (Core)/spinel (Shell) Nanocubes Obtained by Decomposition of Iron Oleate Complex. *J. Colloid Interface Sci.* **2010**, *346*, 37–42.

(34) Chen, C.; Chiang, R.-K.; Lai, H.; Lin, C. Characterization of Monodisperse Wüstite Nanoparticles Following Partial Oxidation. *J. Phys. Chem. C* **2010**, *114*, 4258–4263.

(35) Chen, C.-J.; Chiang, R.-K.; Kamali, S.; Wang, S.-L. Synthesis and Controllable Oxidation of Monodisperse Cobalt-Doped Wüstite Nanoparticles and Their Core-Shell Stability and Exchange-Bias Stabilization. *Nanoscale* **2015**, *7*, 14332–14343.

(36) Estrader, M.; López-Ortega, A.; Estradé, S.; Golosovsky, I. V; Salazar-Alvarez, G.; Vasilakaki, M.; Trohidou, K. N.; Varela, M.; Stanley, D. C.; Sinko, M.; *et al.* Robust Antiferromagnetic Coupling in Hard-Soft Bi-Magnetic Core/shell Nanoparticles. *Nat. Commun.* **2013**, *4*, 2960.

(37) Sytnyk, M.; Kirchschlager, R.; Bodnarchuk, M. I.; Primetzhofer, D.; Kriegner, D.; Enser, H.; Stangl, J.; Bauer, P.; Voith, M.; Hassel, A. W.; *et al.* Tuning the Magnetic Properties of Metal Oxide Nanocrystal Heterostructures by Cation Exchange. *Nano Lett.* **2013**, *13*, 586–593.

(38) Franco, A.; e Silva, F. C. High Temperature Magnetic Properties of Cobalt Ferrite Nanoparticles. *Appl. Phys. Lett.* **2010**, *96*, 172505.

(39) Liu, X. S.; Gu, B. X.; Zhong, W.; Jiang, H. Y.; Du, Y. W. Ferromagnetic/antiferromagnetic Exchange Coupling in SrFe 12 O 19 /CoO Composites. *Appl. Phys. A* **2003**, *77*, 673–676.

(40) Bean, C. P.; Livingston, J. D. Superparamagnetism. *J. Appl. Phys.* **1959**, *30*, S120.

(41) H. P. J. Wijn. *Landolt-Börnstein - Numerical Data and Functional Relationships in Science and Technology, Vol. III/27G (Various Other Oxides)*; Wijn, H. P. J., Ed.; Landolt-Börnstein - Group III Condensed Matter; Springer-Verlag: Berlin/Heidelberg, 1992; Vol. 27G.

(42) Boubel, M. A.; Mainard, R. P.; Fousse, H. G.; Pointon, A. J.; Jeannot, F. R. The Specific Heat Anomaly of Solid Solutions of Isostructural Antiferromagnetic Oxides (pFeO—qCoO). *Phys. Status Solidi (a)* **1976**, *35*, 459–464.

(43) Bracconi, P. Molecular-Field Treatment of the High Temperature Susceptibility and Néel Temperature of Type II Antiferromagnetic Solid-Solutions xNiO−(1−x)CoO. *J. Magn. Magn. Mater.* **1983**, *40*, 37–47.

(44) Mallick, P.; C. Mishra, N. Evolution of Structure, Microstructure, Electrical and Magnetic Properties of Nickel Oxide (NiO) with Transition Metal Ion Doping. *Am. J. Mater. Sci.* **2012**, *2*, 66–71.

(45) Abarra, E. N.; Takano, K.; Hellman, F.; Berkowitz, A. E. Thermodynamic

Measurements of Magnetic Ordering in Antiferromagnetic Superlattices. *Phys. Rev. Lett.* **1996**, *77*, 3451–3454.

(46) Casula, M. F.; Floris, P.; Innocenti, C.; Lascialfari, A.; Marinone, M.; Corti, M.; Sperling, R. a.; Parak, W. J.; Sangregorio, C. Magnetic Resonance Imaging Contrast Agents Based on Iron Oxide Superparamagnetic Ferrofluids. *Chem. Mater.* **2010**, *22*, 1739–1748.

(47) Harres, A.; Mikhov, M.; Skumryev, V.; Andrade, A. M. H. de; Schmidt, J. E.; Geshev, J. Criteria for Saturated Magnetization Loop. *J. Magn. Magn. Mater.* **2016**, *402*, 76–82.

(48) Bodnarchuk, M. I.; Kovalenko, M. V; Groiss, H.; Resel, R.; Reissner, M.; Hesser, G.; Lechner, R. T.; Steiner, W.; Schäffler, F.; Heiss, W. Exchange-Coupled Bimagnetic Wüstite/metal Ferrite Core/shell Nanocrystals: Size, Shape, and Compositional Control. *Small* **2009**, *5*, 2247–2252.

(49) Baaziz, W.; Pichon, B. P.; Liu, Y.; Grenèche, J.-M.; Ulhaq-Bouillet, C.; Terrier, E.; Bergeard, N.; Halté, V.; Boeglin, C.; Choueikani, F.; *et al.* Tuning of Synthesis Conditions by Thermal Decomposition toward Core–Shell Co X Fe 1– X O@Co Y Fe 3– Y O 4 and CoFe 2 O 4 Nanoparticles with Spherical and Cubic Shapes. *Chem. Mater.* **2014**, *26*, 5063–5073.

(50) Lavorato, G. C.; Lima, E.; Troiani, H. E.; Zysler, R. D.; Winkler, E. L. Exchange-Coupling in Thermal Annealed Bimagnetic Core/shell Nanoparticles. *J. Alloy. Compd.* **2015**, *633*, 333–337.

(51) Winkler, E. L.; Lima, E.; Tobia, D.; Saleta, M. E.; Troiani, H. E.; Agostinelli, E.; Fiorani, D.; Zysler, R. D. Origin of Magnetic Anisotropy in ZnO/CoFe2O4 and CoO/CoFe2O4 Core/shell Nanoparticle Systems. *Appl. Phys. Lett.* **2012**, *101*, 252405.

(52) Meiklejohn, W. H. Exchange Anisotropy—A Review. *J. Appl. Phys.* **1962**, *33*, 1328-1335.

(53) Schulthess, T. C.; Butler, W. H. Consequences of Spin-Flop Coupling in Exchange Biased Films. *Phys. Rev. Lett.* **1998**, *81*, 4516–4519.

(54) Lima, E.; Winkler, E. L.; Tobia, D.; Troiani, H. E.; Zysler, R. D.; Agostinelli, E.; Fiorani, D. Bimagnetic CoO Core/CoFe 2 O 4 Shell Nanoparticles: Synthesis and Magnetic Properties. *Chem. Mater.* **2012**, *24*, 512–516.

(55) Coey, J. M. D. *Magnetism and Magnetic Materials*; Cambridge University Press: New York, 2010.

(56) Malozemoff, A. P. Heisenberg-to-Ising Crossover in a Random-Field Model with Uniaxial Anisotropy. *Phys. Rev. B* **1988**, *37*, 7673–7679.

(57) Ali, M.; Marrows, C. H.; Hickey, B. J. Onset of Exchange Bias in Ultrathin Antiferromagnetic Layers. *Phys. Rev. B* **2003**, *67*, 172405.

(58) Shi, Z.; Du, J.; Zhou, S.-M. Exchange Bias in Ferromagnet/antiferromagnet Bilayers. *Chin. Phys. B* **2014**, *23*, 027503.

(59) Vasilakaki, M.; Trohidou, K. N.; Nogués, J. Enhanced Magnetic Properties in Antiferromagnetic-Core/ferrimagnetic-Shell Nanoparticles. *Sci .Rep.* **2015**, *5*, 9609.

(60) Richardson, J. T.; Yiagas, D. I.; Turk, B.; Forster, K.; Twigg, M. V. Origin of

Superparamagnetism in Nickel Oxide. *J. Appl. Phys.* **1991**, *70*, 6977-6982.

(61) Miltényi, P.; Gierlings, M.; Keller, J.; Beschoten, B.; Güntherodt, G.; Nowak, U.; Usadel, K. D. Diluted Antiferromagnets in Exchange Bias: Proof of the Domain State Model. *Phys. Rev. Lett.* **2000**, *84*, 4224–4227.

(62) Takano, K.; Kodama, R. H.; Berkowitz, A. E.; Cao, W.; Thomas, G. Interfacial Uncompensated Antiferromagnetic Spins: Role in Unidirectional Anisotropy in Polycrystalline Ni81Fe19/CoO Bilayers. *Phys. Rev. Lett.* **1997**, *79*, 1130–1133.

(63) Roy, S.; Fitzsimmons, M. R.; Park, S.; Dorn, M.; Petracic, O.; Roshchin, I. V.; Li, Z.-P.; Batlle, X.; Morales, R.; Misra, A.; *et al.* Depth Profile of Uncompensated Spins in an Exchange Bias System. *Phys. Rev. Lett.* **2005**, *95*, 047201.

(64) Kodama, R. H.; Makhlouf, S. A.; Berkowitz, A. E. Finite Size Effects in Antiferromagnetic NiO Nanoparticles. *Phys. Rev. Lett.* **1997**, *79*, 1393–1396.

(65) Cabo, M.; Pellicer, E.; Rossinyol, E.; Estrader, M.; López-Ortega, A.; Nogués, J.; Castell, O.; Suriñach, S.; Baró, M. D. Synthesis of Compositionally Graded Nanocast NiO/NiCo2O4/Co3O4 Mesoporous Composites with Tunable Magnetic Properties. *J. Mater. Chem.* **2010**, *20*, 7021–7028.

(66) Golosovsky, I. V; Salazar-Alvarez, G.; López-Ortega, A.; González, M. A.; Sort, J.; Estrader, M.; Suriñach, S.; Baró, M. D.; Nogués, J. Magnetic Proximity Effect Features in Antiferromagnetic/ferrimagnetic Core-Shell Nanoparticles. *Phys. Rev. Lett.* **2009**, *102*, 247201.

(67) De Toro, J. A.; Marques, D. P.; Muñiz, P.; Skumryev, V.; Sort, J.; Givord, D.; Nogués, J. High Temperature Magnetic Stabilization of Cobalt Nanoparticles by an Antiferromagnetic Proximity Effect. *Phys. Rev. Lett.* **2015**, *115*, 057201.

(68) Leighton, C.; Suhl, H.; Pechan, M. J.; Compton, R.; Nogués, J.; Schuller, I. K. Coercivity Enhancement above the Néel Temperature of an Antiferromagnet/ferromagnet Bilayer. *J. Appl. Phys.* **2002**, *92*, 1483-1488.

(69) Bertoni, G.; Verbeeck, J. Accuracy and Precision in Model Based EELS Quantification. *Ultramicroscopy* **2008**, *108*, 782–790.

(70) Bertoni, G.; Grillo, V.; Brescia, R.; Ke, X.; Bals, S.; Catellani, A.; Li, H.; Manna, L. Direct Determination of Polarity, Faceting, and Core Location in Colloidal Core/Shell Wurtzite Semiconductor Nanocrystals. *ACS Nano* **2012**, *6*, 6453–6461.

(71) Young, R. *The Rietveld Method*; Oxford University Press, 1993.

TABLES

Table 1. *Left: mean diameter (<d>), core diameter (d_{core}), and shell thickness (t_{shell}) obtained from TEM images. Right: cell parameter (a), crystal size (D), weight percentage (w%), core diameter (d_{core}) and shell thickness (t_{shell}) obtained from XRD patterns (rs and s stand for rock-salt and spinel structure, respectively)*

Label	TEM			XRD							
				Rock-Salt Phase (RS)				Spinel Phase (S)			
	<d> (nm)	d_{core} (nm)	t_{shell} (nm)	a_{rs} (nm)	D_{rs} (nm)	$\%_{rs}$ (w%)	d_{core} (nm)	a_s (nm)	D_s (nm)	$\%_s$ (w%)	t_{shell} (nm)
CS6	6 (1)	2	2	0.420	6.3	13	3.2	0.842	2.3	87	1.4
CS9	9 (1)	5	2	0.424	7.4	36	6.6	0.841	2.1	64	1.2
CS15	15 (2)	11	2	0.426	14.0	57	12.6	0.841	2.6	43	1.2
CS18	18 (1)	14	2	0.426	14.8	53	14.8	0.840	3.0	47	1.6

Table 2. *Blocking temperature (T_B), Néel temperature (T_N), coercive field (H_C) and exchange bias (H_E) measured at low temperature (10 K) both in ZFC and FC (120 kOe) conditions.*

Label	T_B (K)	T_N (K)	ZFC		120 kOe FC	
			H_C^{ZFC} (kOe)	H_E^{ZFC} (kOe)	H_C^{FC} (kOe)	H_E^{FC} (kOe)
CS6	115	-	13.5	0	15.0	3.2
CS9	179	223	13.7	0	19.3	8.6
CS15	300	217	12.4	0	16.2	5.5
CS18	380	227	12.6	0	16.3	5.5

FIGURES

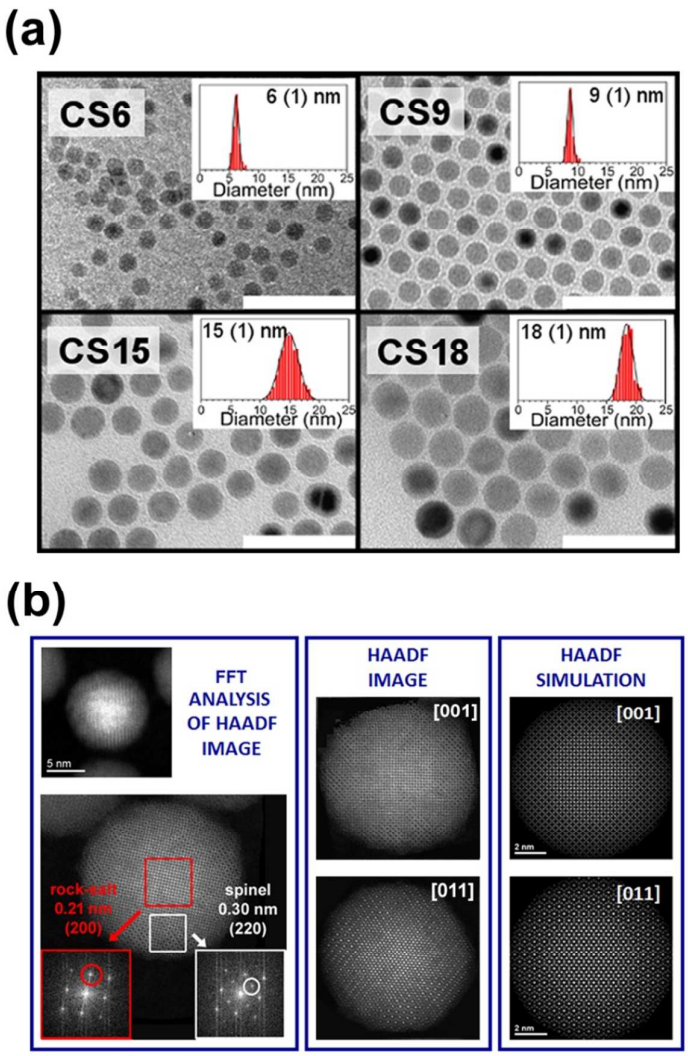

Figure 1. (a) TEM images and corresponding particles size histograms of the series of CS NPs (white scale bars correspond to 50 nm). (b) HAADF images: FFT analysis on the core and shell regions (left) and comparison between HAADF images and HAADF simulations for rock-salt|spinel CS NPs.

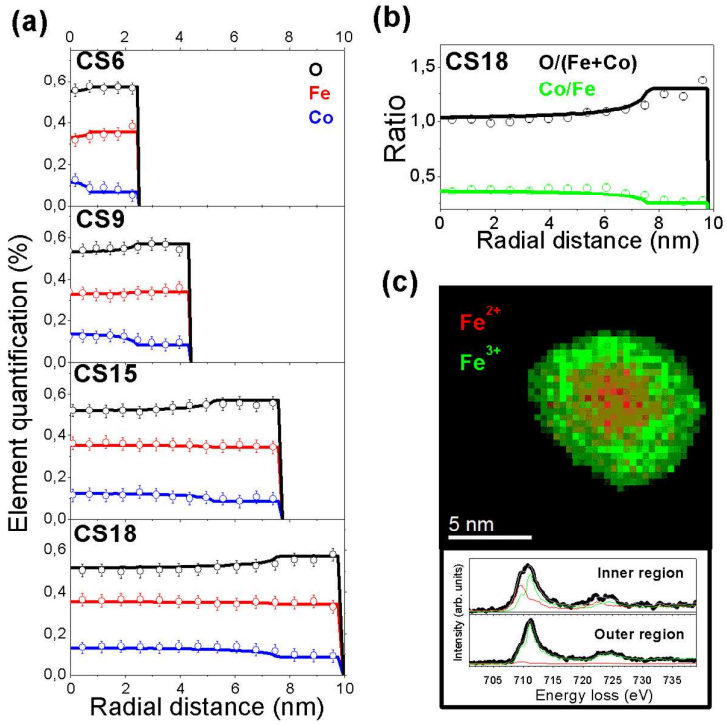

Figure 2. (a) Experimental (symbols) and simulated (lines) EELS profiles for each sample of the series. (b) Experimental oxygen-to-metal and cobalt-to-iron ratios along the NP radius for CS18. The solid line corresponds to the ratio estimated for a CS structure with composition $Co_{0.3}Fe_{0.7}O|Co_{0.6}Fe_{2.4}O_4$ (c) Iron ions mapping across the NP and representative Fe-$L_{2,3}$ spectra from inner (sum of core and shell) and outer (shell) regions of one NP from CS9.

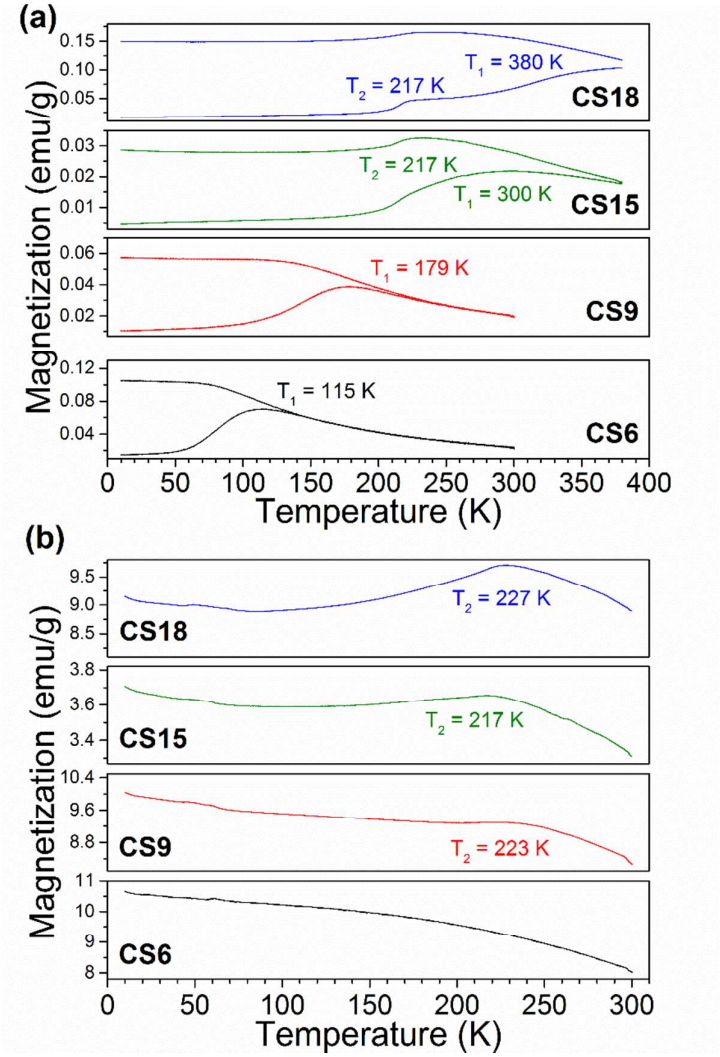

Figure 3. (a) Temperature dependence of the magnetization of CS NPs recorded at 50 Oe after ZFC-FC processes and (b) FC magnetization recorded at 30 kOe.

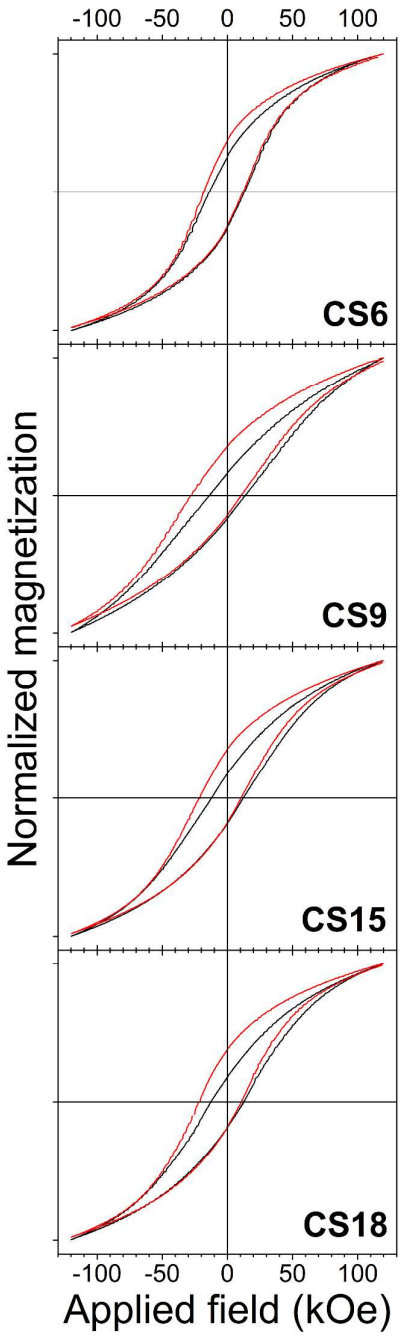

Figure 4. Hysteresis loops at 10 K recorded in a field range of ±120 kOe after ZFC (black) and 120 kOe FC (red) processes.

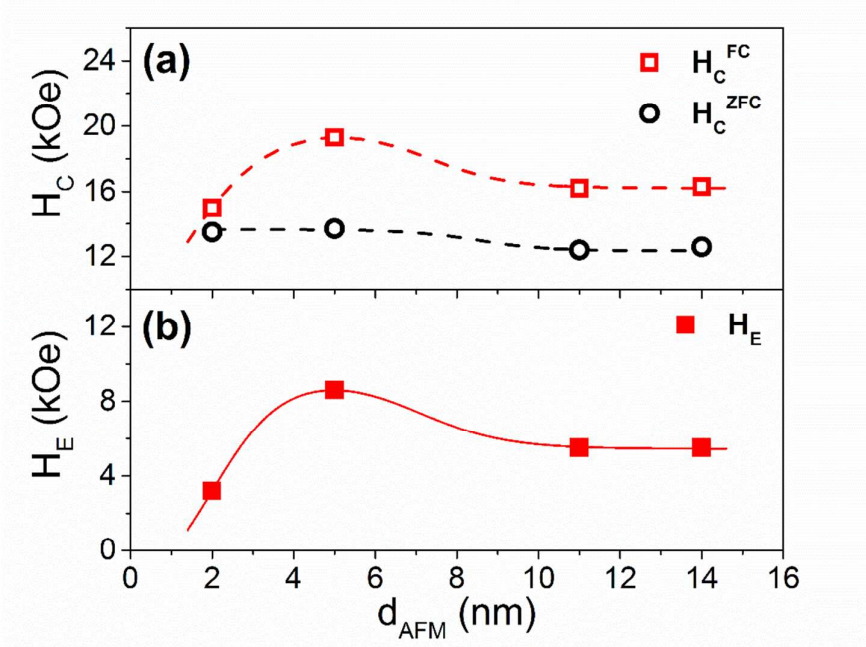

Figure 5. (a) H_C at 10 K as a function of d_{AFM}; H_C values were obtained after FC at 120 kOe (red) or ZFC (black) processes from RT. (b) H_E at 10 K as a function of d_{AFM} after FC at 120 kOe process from RT. (The lines are guides to the eyes).

TA BLE OF CONTENTS GRAPHIC